JOURNAL OF SYNCHROTRON RADIATION
ISSN 1600-5775

Quantitative 4D X-ray microtomography under extreme conditions: a case study on magma migration

Elena Giovenco,[a]* Jean-Philippe Perrillat,[a] Eglantine Boulard,[b] Andrew King,[c] Nicolas Guignot[c] and Yann Le Godec[b]

[a]Laboratoire de Géologie de Lyon, UMR5276, Université Claude Bernard Lyon 1, CNRS, Ens de Lyon, F-69622 Villeurbanne, France, [b]Institut de Minéralogie, de Physique des Matériaux et de Cosmochimie, UMR 7590, Sorbonne Université, CNRS, MNHN, IRD, F-75252 Paris, France, and [c]Synchrotron Soleil, L'Orme des Merisiers, F-91192 St Aubin, France. *Correspondence e-mail: elena.giovenco@univ-lyon1.fr

Received 10 February 2021
Accepted 8 July 2021

Edited by A. Stevenson, Australian Synchrotron, Australia

Keywords: X-ray absorption microtomography; high-pressure–high-temperature; melt migration.

X-ray computed tomography (XCT) is a well known method for three-dimensional characterization of materials that is established as a powerful tool in high-pressure/high-temperature research. The optimization of synchrotron beamlines and the development of fast high-efficiency detectors now allow the addition of a temporal dimension to tomography studies under extreme conditions. Presented here is the experimental setup developed on the PSICHE beamline at SOLEIL to perform high-speed XCT in the Ultra-fast Tomography Paris–Edinburgh cell (UToPEc). The UToPEc is a compact panoramic (165° angular aperture) press optimized for fast tomography that can access 10 GPa and 1700°C. It is installed on a high-speed rotation stage (up to 360° s^{-1}) and allows the acquisition of a full computed tomography (CT) image with micrometre spatial resolution within a second. This marks a major technical breakthrough for time-lapse XCT and the real-time visualization of evolving dynamic systems. In this paper, a practical step-by-step guide to the use of the technique is provided, from the collection of CT images and their reconstruction to performing quantitative analysis, while accounting for the constraints imposed by high-pressure and high-temperature experimentation. The tomographic series allows the tracking of key topological parameters such as phase fractions from 3D volumetric data, and also the evolution of morphological properties (*e.g.* volume, flatness, dip) of each selected entity. The potential of this 4D tomography is illustrated by percolation experiments of carbonate melts within solid silicates, relevant for magma transfers in the Earth's mantle.

1. Introduction

X-ray computed tomography (XCT) is established as a powerful non-destructive method to characterize multiple properties in three dimensions (Maire & Withers, 2014). Recently, this technique has been adapted to high-pressure (HP) research (Guignot *et al.*, 2020) either in triaxial rigs (Renard *et al.*, 2016), large-volume presses (LVP) such as Drickamer (Wang *et al.*, 2005) and Paris–Edinburgh (PE) modules (Philippe *et al.*, 2016), or diamond anvil cells for ultra-high-pressure conditions (Liu *et al.*, 2008; Mao *et al.*, 2019). Major constraints for high-pressure experiments come from the sample-confining environment (*i.e.* pressure medium and anvils) and the equipment size, which mean that the sample is not directly accessible and which restrict the short sample-to-detector distance required for high-resolution imaging. The first LVP used for tomography measurements was a modified Drickamer cell fitted in a 250 ton hydraulic press at GSECARS (Wang *et al.*, 2005). Since then, numerous improvements have been made, including the use of toroidal

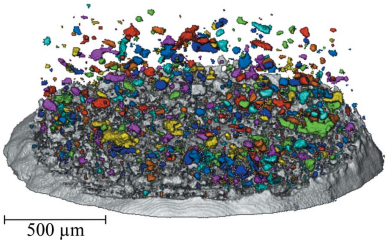

opposed anvils, and attenuation XCT is now routinely performed at up to 8 GPa and 1700°C for various scientific applications (Yu *et al.*, 2016).

To create a more compact experimental setup that is portable enough for use at multiple synchrotron sources, a tomography module was developed for Paris–Edinburgh presses (Philippe *et al.*, 2016). The RoToPEc (Rotating Tomography Paris–Edinburgh cell) allows tomographic studies under high pressure and temperature, up to 10 GPa and 2200°C with conventional tungsten carbide anvils, in either absorption or diffraction scattering mode (Álvarez-Murga *et al.*, 2017; Boulard *et al.*, 2020). Both systems rely on rotating anvils supported by thrust bearings inside the load frame and require the use of X-ray transparent containment rings and cell assemblies so that the sample can be imaged over 360°. Despite the development of these techniques, the range of application is limited by the rotation speed of the anvils. Indeed, XCT tomographs are typically recorded in 20 min or more, making tomographic reconstruction impossible if the sample undergoes significant plastic deformation or structural or chemical changes during the acquisition of the projection images. Dynamic processes with second to minute characteristic times are thus inaccessible.

To overcome this limitation, a Paris–Edinburgh press optimized for fast tomography has been developed, the UToPEc (Ultra-fast Tomography Paris–Edinburgh cell; Boulard *et al.*, 2018). Based on a modified two-column press (Klotz *et al.*, 2004), the UToPEc is compact (Ø 170 mm, 20 kg) and can be installed on a high-speed rotation stage for continuous image acquisition. It is designed with a large 165° angular opening, and hence offers limited blind angles that can be tolerated or corrected for by reconstruction algorithms (Turpin *et al.*, 2020). Pressures and temperatures up to 10 GPa and 1700°C can be targeted with a micrometric spatial resolution for 3D volumes recorded in less than 1 s at full rotation speed.

In this paper, we present the specific details of a high-pressure tomography experiment as a practical step-by-step guide to using the apparatus, from experimental setup to possible results, by detailing the acquisition, reconstruction, segmentation and quantification procedures. The interest of such temporal resolution is shown by the example of the migration of carbonate-rich melts in the Earth's upper mantle. This case study illustrates fluid percolation monitoring through characterization of flow dynamics and geometry, as well as the morphological tracking of entities.

2. Experimental setup

2.1. X-ray tomography setup on the PSICHE beamline

XCT experiments were conducted on the high-pressure beamline PSICHE at the Synchrotron SOLEIL (King *et al.*, 2019; Fig. 1). A high-flux parallel X-ray beam with a mean energy of around 45 keV is produced by filtering the polychromatic source using metal filters and an X-ray mirror ('pink' beam illumination), providing a 3 mm × 1.5 mm field of view and a fast exposure time. Transmitted images are converted into visible light by a 100 µm thick LuAg scintillator screen coupled by a microscope objective lens to a PCO Dimax CMOS high-speed camera (pco.dimax HS4, PCO AG, Germany; https://www.pco.de/highspeed-cameras/pcodimax-hs4/) capable of recording more than 2000 full images per

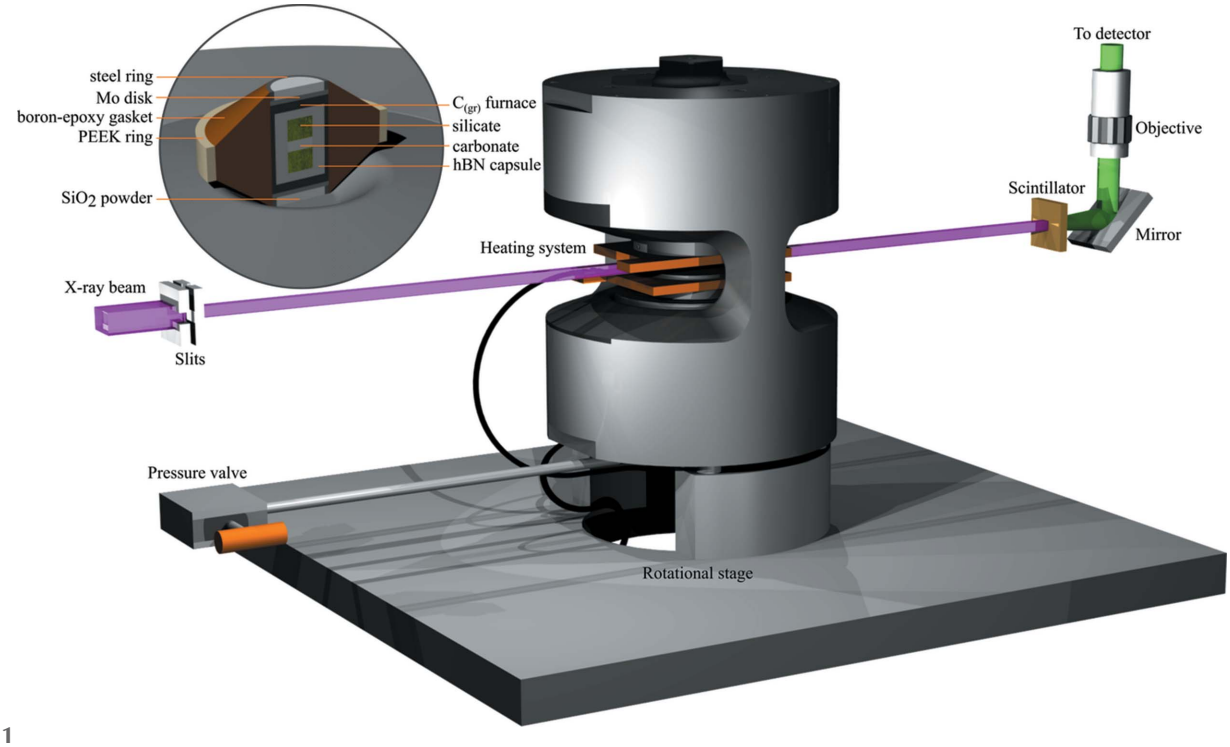

Figure 1
The UToPEc setup used in parallel pink-beam XCT configuration and PE assembly with 'sandwich' configuration starting sample.

Table 1
A summary of experimental conditions and data acquisition.

LT stands for latency time, corresponding to the time delay between cycles. Duration corresponds to the total amount of time above the melting point. Cycles of 12 and 15 tomographs last more than ∼3 min and ∼4 min, respectively. The pressure was calculated from hBN cell parameters and the equation of state of Le Godec *et al.* (2000). The temperature was estimated using a power–temperature relation curve determined in a previous experiment using a thermocouple.

		Cycle 1			Cycle 2			Cycle 3			
Sample name	$P_{initial}$ (GPa)	T (°C)	No. of tomographs	LT (min)	T (°C)	No. of tomographs	LT (min)	T (°C)	No. of tomographs	Duration (min)	P_{final} (GPa)
BaCarb1	2.0	890	12	12	890	12	30	890	12	62	0.45
BaCarb3	1.6	830	15	11	955	15	15	1040	15	42	0.50

second. High-temperature and high-pressure conditions were achieved using the UToPEc press. The small size of the press allows the sample-to-detector distance to be reduced and hence a better spatial resolution can be achieved by reducing blurring due to beam divergence. Using a 7.5× optical magnification results in an effective pixel size of 1.47 µm, with 4–5 µm true resolution in the reconstruction (King *et al.*, 2019).

The UToPEc is mounted on *x*–*y*–*z* translational and rotational stages using rotary couplings that allow a continuous rotation of the press at up to 360° s^{-1} while maintaining the electrical current and hydraulic cooling supplies (Guignot *et al.*, 2020). To date, the hydraulic oil is not yet connected via rotary joints; the pressure must be adjusted prior to the tomographic acquisition, and then a valve seals the system while the oil pump is disconnected. The setup is also compatible with X-ray diffraction, which was used for the measurement of pressure using an hBN-based calibration (Le Godec *et al.*, 2000).

2.2. Time-resolved XCT experiments

An experiment was designed to study the percolation of a liquid carbonate phase through an aggregate of solid silicate grains. Starting materials consisted of a 0.4–0.6 mm thick layer of barium carbonate ($BaCO_3$ nano-powder from Alfa Aesar) enclosed between two layers of polycrystalline olivine $Mg_{0.9}Fe_{0.1}Si_2O_4$ powder (Fig. 1). The micrometre-sized (∅ < 100 µm) olivine grains were sorted from a natural San Carlos peridotite specimen, and included sporadic iron oxides and pyroxenes as impurities. $BaCO_3$ heavy carbonate was chosen as the percolating liquid to enhance its X-ray absorption contrast with the olivine solid matrix. Tungsten carbide (WC) spheres were also embedded within the olivine powder as positional reference markers (the need for these will be further explained in Section 3.1). These 'sandwich' samples were loaded in a classical PE assembly (Perrillat, 2008) with a hexagonal boron nitride (hBN) capsule, graphite furnace, 10 mm boron epoxy gasket and poly(ether ether ketone) (PEEK) containment ring (Fig. 1).

Samples were first pressurized to 2 GPa. This cold compression stage led to a strong reduction of the olivine powder's initial porosity to achieve a value of 5–10%. The temperature was then increased in steps above the melting point of $BaCO_3$ ($T > 800$°C) for computed tomography (CT) imaging of liquid migration. The entire process under extreme conditions lasted over one hour, after which the samples were quenched and prepared for SEM observations. Table 1 summarizes the *P*–*T* conditions and XCT acquisition characteristics for the studied samples, BaCarb1 and BaCarb3.

The real-time monitoring of $BaCO_3$ liquid migration was limited over time by the capacity of the on-board memory of the CMOS camera and the duration of data transfer to the storage network. For the field of view needed in this experiment, *i.e.* the whole gap between the anvils, a maximum of approximately 15 000 projections (1500 × 1500 pixels) could be recorded, corresponding to about 15 CT images. The data transfer to the storage network of the projections corresponding to a single CT image took approximately 1 min. In order to capture the motion of the carbonate liquid, with second to minute resolution, we defined a sequence of 12–15 CT scans, each of 1 s duration with a 15 s interval between each tomograph. Data were downloaded from the camera after each sequence (transfer took about 10–15 min). Dark- and flat-field images were recorded at the beginning and end of each sequence as the spatial inhomogeneity of the incident beam, scintillator and CMOS response are stable over such a short period (< 4 min). Three such cycles were performed for each sample (see Table 1).

3. Analysis methods

3.1. CT image reconstruction and pre-treatment

Each tomograph consisted of 900 projections recorded over 180° rotation in 1.035 s. Volume reconstruction was performed via standard filtered backprojection using *PyHST2* (Mirone *et al.*, 2014) and applying a flat-field correction and Paganin phase retrieval (Paganin *et al.*, 2002). After removing partially truncated projections, the presence of 15° missing angles did not produce noticeable artefacts affecting the volume quality, as already observed by Urakawa *et al.* (2010) and Boulard *et al.* (2018).

After reconstruction, the data corresponded to stacks of *XY* slices in 32 bit floating format. These were converted into 8 bit integer format to reduce memory requirements and facilitate their analysis. This conversion was performed using *ImageJ* (Rasband, 1997–2018) from the greyscale histograms within

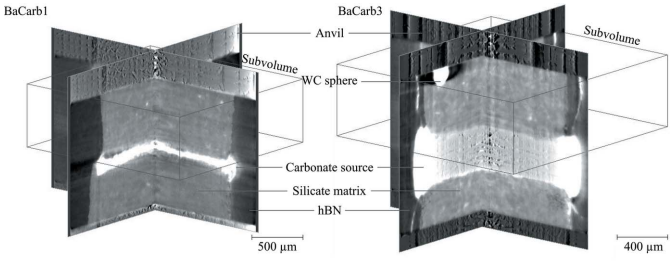

Figure 2
Tomography cross sections with studied subvolume representation. The illustrated cross sections are from the last CT images of cycle 3 for both samples BaCarb1 and BaCarb3 (see Table 1 for more details).

the olivine matrix. The display range values of the 32 bit images were restricted to the most represented values to enhance greyscale repartition and thus interstitial carbonate visibility during the linear scaling. These display ranges were kept constant for all tomographs. Thus small numbers of voxels became saturated (0 or 255), as was visible later on the 8 bit histogram (Fig. 3) used for thresholding. Representative subvolumes were then extracted to reduce the calculation time during segmentation and post-processing, with dimensions of 1275 × 1325 × 435 voxels (∼1875 µm × 1948 µm × 639 µm) for BaCarb1 and 1300 × 1250 × 402 voxels (∼1911 µm × 1838 µm × 591 µm) for BaCarb3 (see Fig. 2 for an illustration).

In order to make quantitative comparisons between successive tomographs, the 3D datasets must be spatially aligned. Inherent issues from the high-pressure experiments must be addressed. First, at high temperature, despite the PEEK containment ring, the experimental assembly flows and induces a translation of the sample along the vertical axis as well as a reduction of the gap between the anvils. We used WC sphere markers embedded in the olivine sample to correct for this absolute motion. These benchmarks also confirm that plastic deformation did not occur within the polycrystalline aggregate under high pressure and temperature since the distances between the markers remained constant. Secondly, due to the continuous rotation of the press and the delay between successive CT scans, an angular jitter is observed between tomographs within the same acquisition cycle and between different cycles. This misalignment results in a rotation offset between each data set that can reach 20°. To correct it, 3D volumes are rotated into alignment using a Python script that calculates the barycentre (*i.e.* the centre of mass of entity-associated voxels) of the markers. After these corrections, subvolumes can be overlapped and are thus suitable for subsequent segmentation and quantification.

3.2. CT image segmentation

After conversion to 8 bit integer format, each voxel in the subvolume is characterized by a greyscale value, from 0 to 255, that reflects the local X-ray attenuation coefficient. Here highly absorbent elements, such as $BaCO_3$, appear brighter on the CT slices relative to silicate grains [Fig. 3(*b*)]. Segmentation enables the isolation of voxels with particular intensity

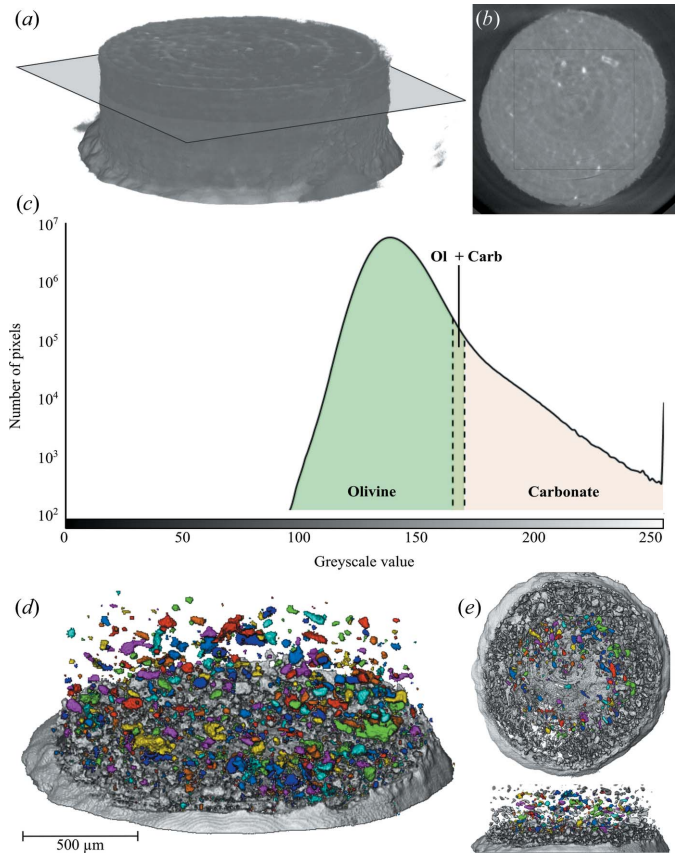

Figure 3
Visualization of the X-ray CT data. (*a*) A view of the BaCarb1 subvolume. (*b*) A representative tomography slice of the olivine polycrystals impregnated by $BaCO_3$ (bright areas). (*c*) A histogram of greyscale values of the 1100 µm × 1100 µm × 325 µm subvolume within the polycrystalline matrix [see squared area in panel (*b*)]. Representative greyscale values of 'olivine' and 'carbonate' are indicated. Values between 0 and 100 correspond to the sample environment and are thus not represented in the subvolume. (*d*) Segmented carbonate blobs after hysteresis thresholding. The position and shape properties of each entity are computed. (*e*) Only coloured entities are studied.

values and their assignment to a phase, either carbonate or olivine silicate. This segmentation step was performed with the ThermoScientific *Avizo* software (Thermo Fisher Scientific, Waltham, MA, USA), using a user-controlled hysteresis thresholding. It consists of a dual thresholding operation, where the first threshold (upper value) determines high-confidence areas (any pixel value above it will be undeniably associated with carbonate) while the second threshold (lower value) consists of an extension of those areas (areas above this threshold are considered to be carbonate if they are connected to high confidence areas). Both threshold values were determined from the greyscale histogram [Fig. 3(*c*)] and were kept constant for each tomography sequence.

The choice of these threshold values is the main source of uncertainty on estimates of carbonate versus silicate volumes, since the projection grey level can fluctuate slightly between CT images. We assess this uncertainty by running multiple segmentations with the same first threshold value but varying the second threshold by ± 2 grey levels. This range corre-

sponds to the eye-estimated reasonable range of values for the extension of the high-confidence limit, as above 2 some carbonate information is not taken into account and below −2 segmentation noise and tomographic reconstruction artefacts are enhanced. In Section 4.1 these uncertainties are represented as envelopes and used to select the CT scans to be compared.

After segmentation, the slices are binary images where 0 corresponds to the silicate matrix and 1 to carbonate elements. Segmented entities not related to the $BaCO_3$ liquid migration, like the WC markers or the carbonate source layer, that are far bigger than target melt pockets, are removed using a filter based on a volume limit. For each carbonate entity in the subvolume, identified as labelled blobs, we computed its position and morphological characteristics [volume, Feret distances (length and thickness), flatness and orientation] using the *Avizo* predefined functions (`BaryCenterX`, `BaryCenterY`, `BaryCenterZ`, `Volume3d`, `Length3d`, `LengthOrientTheta`, `LengthOrientPhi`, `Width3d`, `WidthOrientTheta`, `WidthOrientPhi`).

Using the positional barycentre information, cylindrical regions of interest (ROIs) within the subvolumes were defined to avoid edge defects (*e.g.* liquid flow along the edges of the capsule). All entities whose barycentre is included in the cylinder will be kept in their entirety, so that blobs located at the boundary of an ROI are not cropped. The ROI characteristics for BaCarb1 and BaCarb3 are 294 µm height and 558 µm radius, and 367.5 µm height and 441 µm radius, respectively [Fig. 3(*e*)].

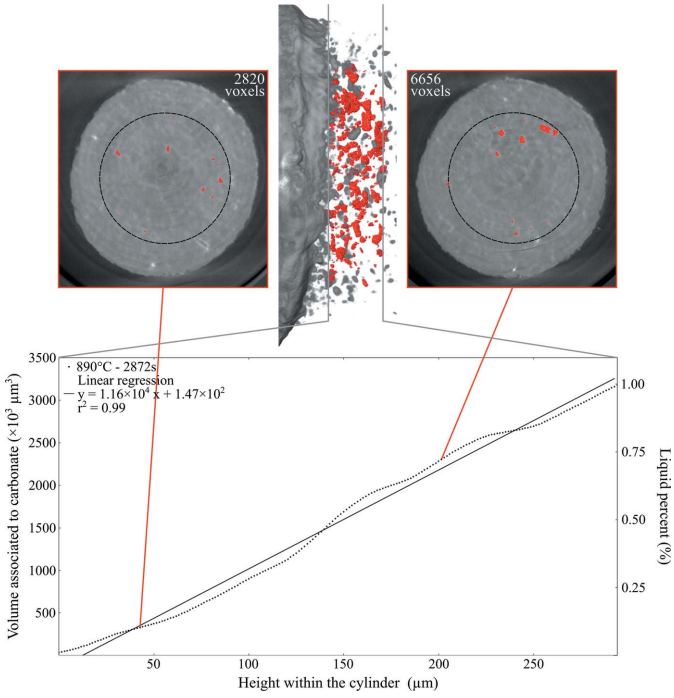

Figure 4
Quantification of flow dynamics, counting every segmented voxel within the cylindrical ROI (dashed line) and studying its cumulative curve for one XCT. Both tomography slices illustrate the number of counted voxels (given the 1.47 µm^3 voxel size, 2820 voxels correspond to ∼9000 µm^3 and 6656 voxels to ∼21 000 µm^3). The left-hand axis displays the absolute volume associated with the voxel count and the right-hand axis represents its comparison with the ROI volume. In this example, 1% of the total volume is segmented as carbonate.

3.3. Flow quantification

The time resolution of 16 s between successive tomographs enables real-time monitoring of the porosity impregnation by $BaCO_3$ liquid, which starts soon after carbonate melting. A simple way to quantify this flow is to track the migration front, *i.e.* the maximal height where fluids are detected along the z axis, for each CT image. To further estimate the 3D volumetric distribution of liquid over time, the carbonate voxels for each slice were summed along the z axis. The obtained cumulative curve (Fig. 4) depicts the contribution of each z slice to the total amount of liquid. If a linear relation is observed, then the carbonate content is constant regardless of the vertical position in the sample and the slope provides a volumetric flow rate (see Section 4.1).

3.4. Object-based analysis

For better constraint of the geometric characteristics of the flow, 3D data can be studied for each segmented entity. Within the cylindrical ROI, the number of carbonate melt pockets varies between 100 and 300. They were investigated in terms of volume, shape and inclination statistics, as well as entity tracking. The following paragraphs and Fig. 5 describe briefly the calculation of these parameters.

3.4.1. Shape analysis. The shape of the blob was characterized using the Feret minimal and maximal diameter. The Feret diameter is a measure of an object's size along a specified direction. It can be defined as the distance between two parallel tangents to the contour of the object. Distances were computed along with a series of orientations, Θ and φ, varying from 0 to 180° and −90 to 90°, respectively, with an interval of 1°. The Feret minimal and maximal distances characterize an entity's thickness (shortest distance) and length (longest distance), respectively. In terms of aspect ratio, an entity's flatness can be computed from $1 - (F_{min}/F_{max})$, such that 0 corresponds to a sphere and 1 to a plane.

3.4.2. Entity inclination. Orientation statistics were obtained on elongated $BaCO_3$ blobs (aspect ratio above 2:1) by measuring their dip angle relative to the XY plane of the subvolume. Inclination statistics are represented by rose diagrams (Fig. 10) and reveal the orientation of melt pockets between solid grains.

3.4.3. Tracking. The 3D alignment of tomographs (see Section 3.1) enables tracking of melt pockets between successive CT images. In this way, the morphological evolution of each entity, identified by its barycentre, can be quantified using the above-defined volume, shape and orientation parameters. Nevertheless, depending on which specific object is considered, entities could disappear, split or merge (either physically or due to data resolution). In consequence, this approach is limited to a restricted set of entities of interest. An example of melt-pocket tracking is shown in Fig. 12 and discussed in Section 4.3.

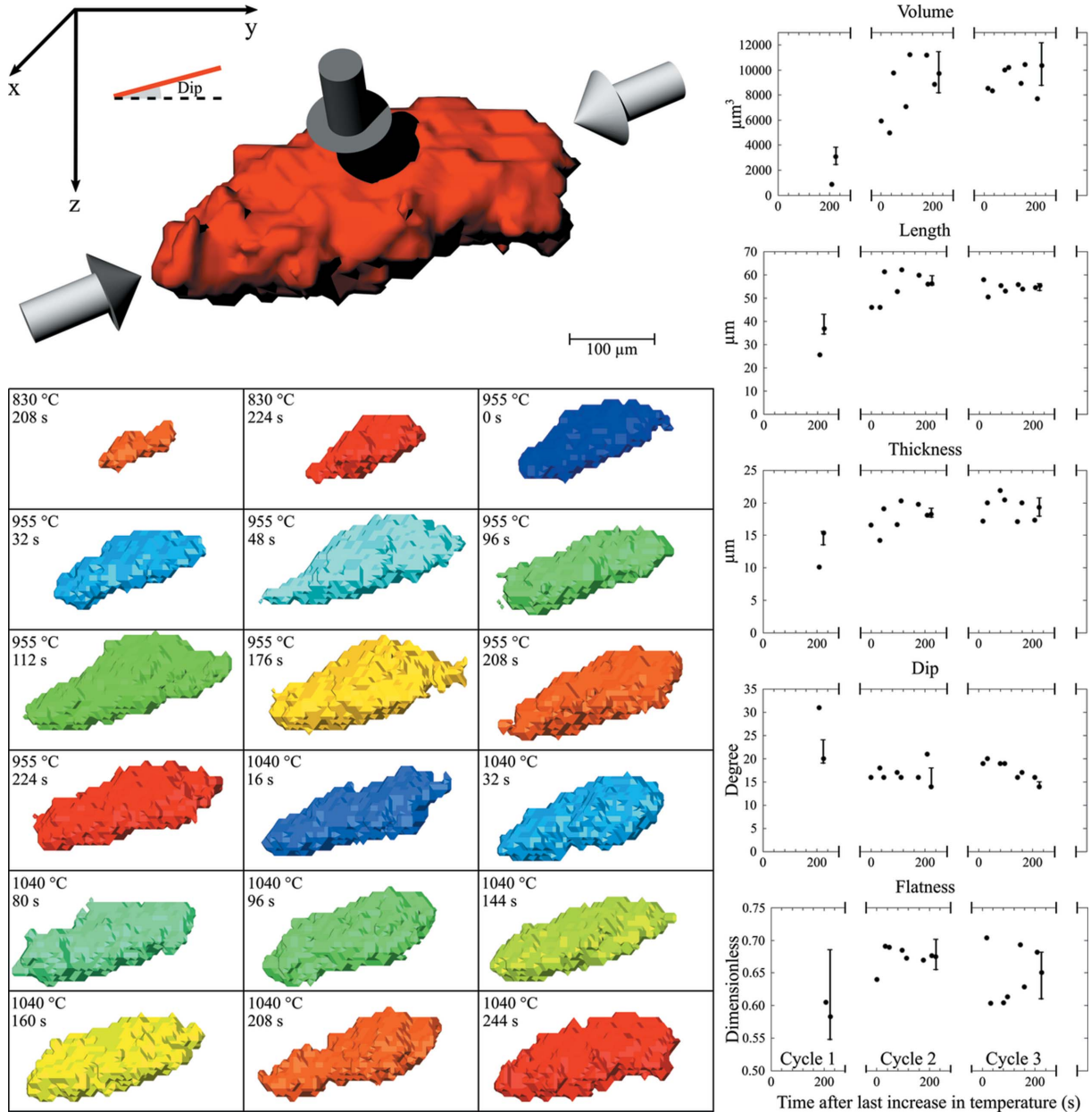

Figure 5
An example of object-based analysis. The upper left-hand figure represents a carbonate entity from the BaCarb3 sample. Its length can be visualized along the white arrows and its thickness along the grey ones. Its dip is measured in the orthogonal system defined by the subvolume. The lower left-hand figures illustrate the morphological evolution of this entity over time, as tracked by time-lapse CT scans. On the right-hand side, the graphs show the evolution of the studied geometric parameters along the three different temperature cycles. The increase in length and thickness of the pocket depicts the growing volume of melt over time, while the dip angle and flatness parameters remain more or less constant.

4. Results and discussion

4.1. Impregnation rate and dynamic

In both experiments BaCarb1 and BaCarb3, the liquid impregnation started as soon as the melting temperature was crossed, as shown by the appearance of melt pockets away from the initial carbonate layer as early as the first tomograph. Subsequent CT images allow the progression of the migration front to be tracked with a 16 s resolution. Fig. 6 shows eight reconstructions recorded for sample BaCarb1 in the first 176 s of experiment and the distribution of carbonate voxels along the z axis (where 0 represents the position of the cylinder ROI basal section) for each CT reconstruction. The progression of the porosity infill by carbonate is clear between the 48, 80, 96 and 112 s CT images to reach the top end of the ROI. In this way, we can estimate that initial impregnation took place over a distance of at least 115 µm between CT scans recorded at 48 and 120 s, which translates into an average vertical rate of 5.35 mm h^{-1}.

In sample BaCarb3, tracking of this impregnation front was made difficult by the presence of sporadic oxide impurities in the olivine powder that bias the identification of small newly

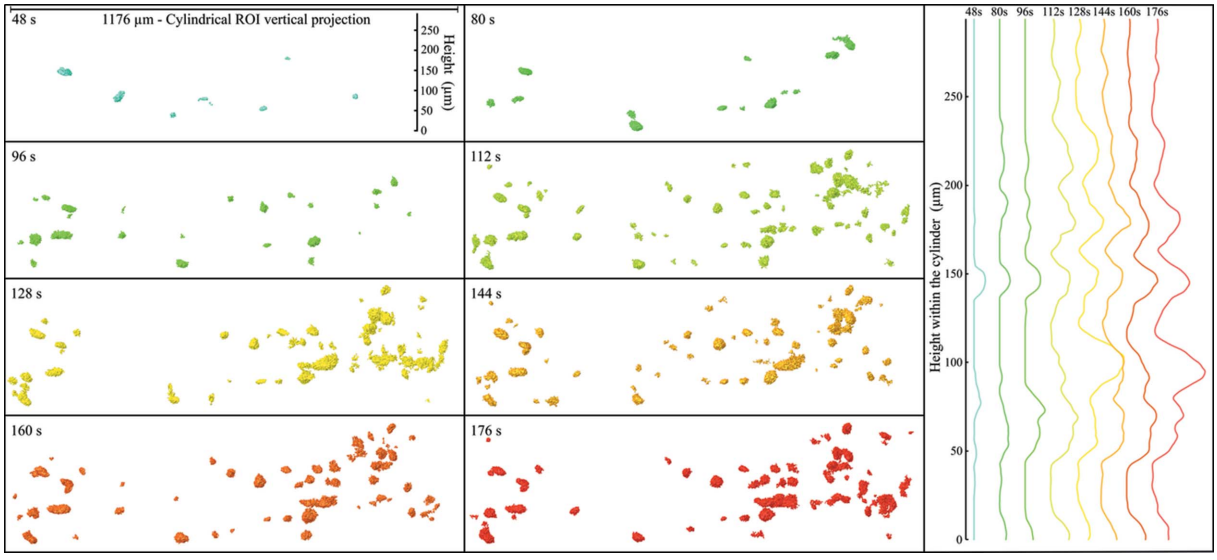

Figure 6
A visualization of the carbonate melt impregnation front in sample BaCarb1. Vertical projections of the cylindrical ROI are represented for eight tomographs over time. The carbonate source is located below the bottom of the image. With time, the melt blobs become more numerous and are located further from the initial layer. The plot on the right-hand side shows the distribution (arbitrary units) of voxels segmented as carbonate along the ROI. Once a porosity is filled, the elongation, flatness and dip of the associated pocket remain relatively constant over time as its volume grows.

formed melt pockets. However, on the last CT image recorded after 224 s, the $BaCO_3$ melt is well dispersed and reached the top end of the ROI. As the sample maximum observable height was 367.5 µm, a mean impregnation rate of 5.91 mm h^{-1} can be estimated.

These impregnation rates can be compared with scanning electron microscopy (SEM) observations on the quenched samples. Given that the experiments lasted about one hour over the melting temperature (62 min for BaCarb1 and 42 min for BaCarb3) and that $BaCO_3$ liquid is observed over the entire 0.9–1 mm thick olivine matrix on the SEM images, we obtain average rates of 1 mm h^{-1} for BaCarb1 and 1.35 mm h^{-1} for BaCarb3. As expected, these estimates are significantly lower than the *in situ* measurements, highlighting the need for time-resolved analyses.

The evolution of the volumetric flow rate as a function of time and temperature is quantified from the distribution of carbonate blobs on successive reconstructions. All cumulative carbonate curves (see Section 3.3) obtained for each CT image for both samples show a linear trend (r^2 for cycles 2 and 3 are > 0.98 for BaCarb1 and > 0.93 for BaCarb3), meaning that the carbonate input is constant regardless of the vertical position in the sample (Fig. 7). Nevertheless, the different slopes between each reconstruction imply different carbonate contents.

A CT image can be modelled as a pile of *XY* slices crossed by a uniaxial vertical flow of carbonate voxels. The volumetric flow rate Q_v, *i.e.* the volume of $BaCO_3$ melt which passes per unit time through a defined slice, is calculated from mass balances between successive CT images according to

$$Q_v = \frac{1}{dt}\left[(S_{t+dt} - S_t)dl + (V_{t+dt} - V_t)\right], \quad (1)$$

where dt is the time interval between CT images, $(S_{t+dt} - S_t)dl$ the cumulative carbonate volume within the defined slice (in our case, the basal section, one voxel thick, of the cylindrical ROI) and $(V_{t+dt} - V_t)$ the volume of carbonate that passed through it (obtained from the above slices of the ROI).

The BaCarb1 images depict the evolution of flow rate as a function of time, as the temperature was constant at 890°C during the whole of the experiment. Flow rates of 4026^{+1936}_{-1378} (where subscript and superscript values correspond to the asymmetric errors), 1130^{+478}_{-358} and 705^{+227}_{-200} µm^3 s^{-1} were calculated between the 96 and 176 s, 176 and 928 s, and 928 and 2904 s CT images, respectively. This decrease in flow rates (Fig. 8) shows that the melt impregnation becomes less effective with time. Conversely, in BaCarb3, the temperature was increased in steps between each CT imaging sequence. Each temperature step was associated with a boost in carbonate flow, as shown by the quick slope increase of the first cumulative curve of each series (Fig. 7). Flow rates were thus calculated between the first and last images of a sequence, giving flow rates of 266^{+354}_{-39} µm^3 s^{-1} for cycle 1 at 830°C, 3731^{+5315}_{-647} µm^3 s^{-1} for cycle 2 at 955°C and 5350^{+8369}_{-1954} µm^3 s^{-1} for cycle 3 at 1040°C. As expected, the flow rates increase with increasing temperature, but not linearly since the porosity is being filled during the cycles.

These observed flow-rate behaviours are characteristic of capillary penetration and fluid transport through porous structures. Indeed, the progression of the wetting front and the decrease in flow rates with time reflect the typical diffusive behaviour of capillary flow (Washburn, 1921). Similarly, the increase in flow rates with temperature highlights the increased diffusivities (*i.e.* lower viscosities) of carbonate melts at high temperature.

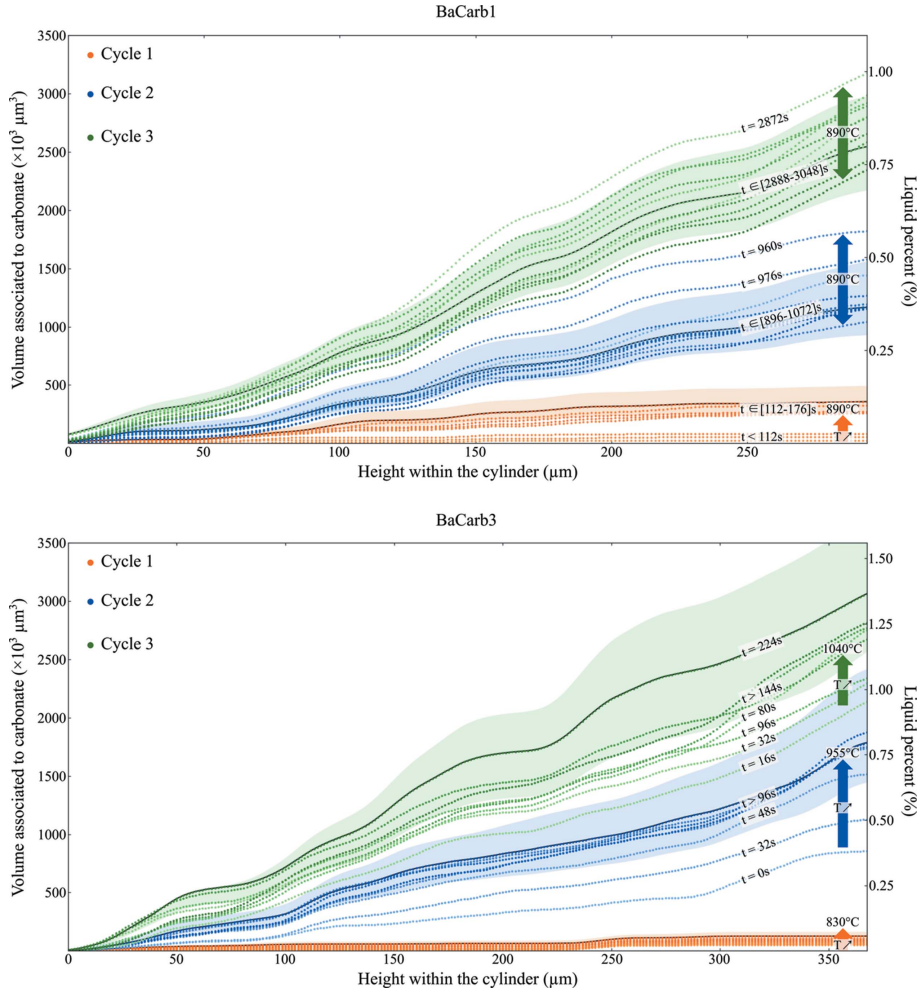

Figure 7
Cumulative curves of carbonate voxels measured for each CT image of successive cycles 1 (in orange), 2 (in blue) and 3 (in green) for both samples BaCarb1 and BaCarb3. In one cycle curve the colours go from light to dark as the times increase. Uncertainties are represented by the shaded region for one tomograph (black line) for each cycle.

4.2. Entity morphology

The evolution of the melt network during impregnation can be addressed by following the morphology of carbonate entities. A sorting of the $BaCO_3$ blobs as a function of their volumes (Fig. 9) reveals a gradual rise in the number of blobs for each size class and a higher representation of large blobs ($> 12\,500\ \mu m^3$) over time, for both the BaCarb1 and BaCarb3 runs. This gradual infill is consistent with an increasing saturation of the porosity after the initial wetting of olivine grain boundaries by the melt front. The melt flow is accommodated by a homogeneous growth of the melt pockets, as illustrated by the jump in pocket size classes and the rise in small melt entities ($< 1250\ \mu m^3$), previously under the detection limit, between successive CT images.

Analysis of the Feret distances and shape ratio (*i.e.* flatness) leads to similar conclusions. The increase in Feret distances with time reflects the homogeneous growth of the melt entities, and their aspect ratios remain constant with a Gaussian distribution centred on 0.5 (*i.e.* on average the thickness is half the length of the blobs, with extrema ratios of 1:5 and 4:5), independent of the pocket size. The orientations of entities estimated from the dip angle relative to the *XY* plane do not show significant variations from the first to the last tomograph, with preferred distribution at angles less than 50°, as shown in the rose diagrams (Fig. 10). These morphological parameters are in agreement with the gradual saturation of the porosity network by $BaCO_3$ liquid.

4.3. Implication for carbonate liquid impregnation process

Knowledge of the location and transport of magmas in the deep Earth is an important step toward the understanding of geochemical and geodynamic processes at depth. It is of primary importance for carbon-rich melts as carbonate magmas impact the deep carbon cycle, which remains highly debated. These carbonate magmas have unique properties, clearly distinct from the widespread silicate liquids, coming from their unpolymerized ionic structure. Due to the weak cohesion of carbonate molecules, these magmas have low viscosities ($< 10^{-2}$ Pa s; Dobson *et al.*, 1996; Kono *et al.*, 2014). This high mobility is reinforced by wetting angles lower than 30° (Hunter & McKenzie, 1989) and a large buoyancy relative to the surrounding mantle rocks (Dobson *et al.*, 1996). Hence,

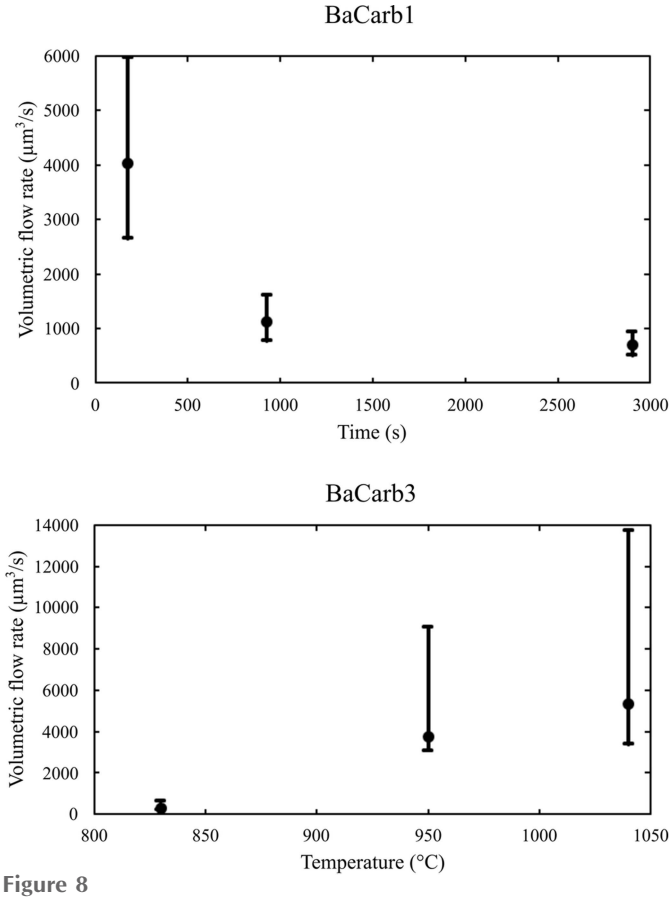

Figure 8
Volumetric flow rates calculated at the cylindrical ROI base from mass-balance models.

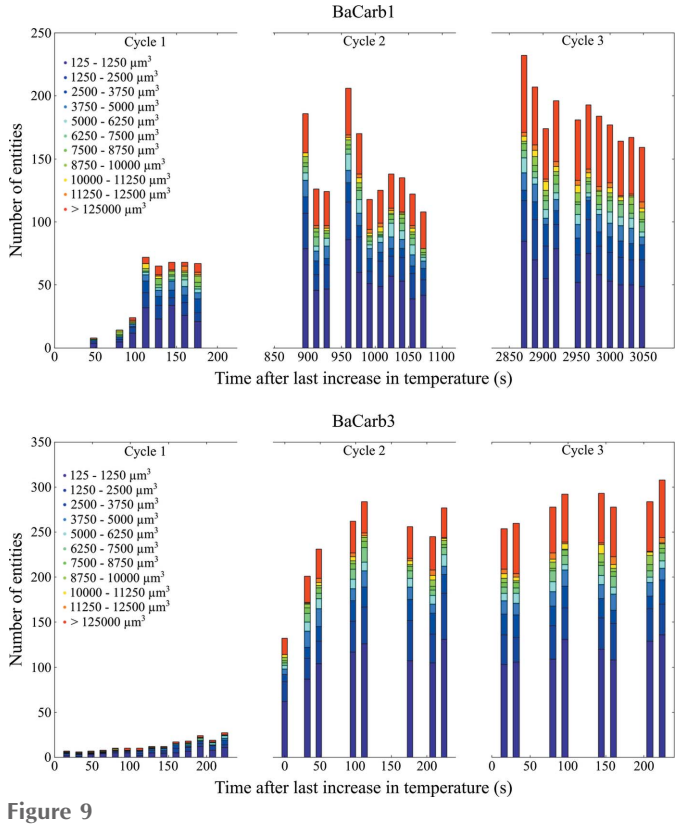

Figure 9
Cumulative histograms for samples BaCarb1 and BaCarb3, displaying the repartition of carbonate entities in volume categories (as colour labelled) during the experiments.

these liquids are expected to form interconnected networks and to be efficiently extracted even at low melt fractions. From a chemical point of view, this large connectivity along grains implies an important exchange surface that makes them highly reactive agents (Green & Wallace, 1988).

Melt migration is often studied regarding buoyancy forces and external pressure gradients. However, capillary forces and associated surface tension effects can also drive magma displacement over geologically relevant distances, particularly for low-viscosity fluids (Stevenson, 1986). As revealed by our experiments, capillary forces cause the molten carbonate to infiltrate the polycrystalline olivine. The melt migrates from high-concentration areas (close to the carbonate source layer) to lower-concentration areas, as illustrated in Fig. 11. This spatial variation in the melt fraction gives rise to a gradient in the effective pressure of the melt, thus providing a thermodynamic driving force for melt migration.

The kinetics of melt infiltration estimated from time-lapse CT images (Fig. 8) exhibit the diffusive dynamics of capillary flow with a decrease in flow rate with time and a positive dependence on temperature. The observed vertical infiltration rates of 5.3–5.9 mm h^{-1} confirm the high mobility of carbonate liquids relative to silicate ones, as already pointed out by Hammouda & Laporte (2000). For comparison, Watson *et al.* (1982) reported infiltration rates of ∼0.05 mm h^{-1} for basaltic silicate liquids under ∼1 GPa and ∼1300°C, *i.e.* about two orders of magnitude slower. The present infiltration rates are slightly faster than the value of ∼2.5 mm h^{-1} reported by Hammouda & Laporte (2000) for sodium carbonate impregnation through a synthetic dunite. This may arise from the time resolution of the present *in situ* measurements that enables us to capture the fast initial propagation front, while the infiltration rate is averaged over the duration of a run in the quench experiments of Hammouda & Laporte (2000). Differences in initial porosity and carbonate melt chemistry ($BaCO_3$ versus Na_2CO_3) may also have a significant effect.

The choice of $BaCO_3$ as the starting material was dictated by the need to enhance the X-ray absorption contrast of the liquid with the olivine matrix. Nevertheless, this led to a carbonate liquid in strong disequilibrium with the solid crystals, and hence to potential chemical exchanges between the $BaCO_3$ melt and the matrix during the flow. This chemical reactivity was indeed observed on the CT images as rims of bright voxels surrounding specific grains (5–10 grains on average in each ROI), subsequently identified as pyroxene impurities using SEM images. Fig. 12 shows the tracking of such a reaction rim and its growth over time, and highlights the fast kinetics of the chemical reaction occurring on a timescale comparable with the melt flow. This points to the need for building reactive transport models for carbonate migration in order to address the interplay between chemical reaction and the physics of melt transport. From this perspective, the extension of 4D microtomography imaging (*e.g.* Dobson *et al.*,

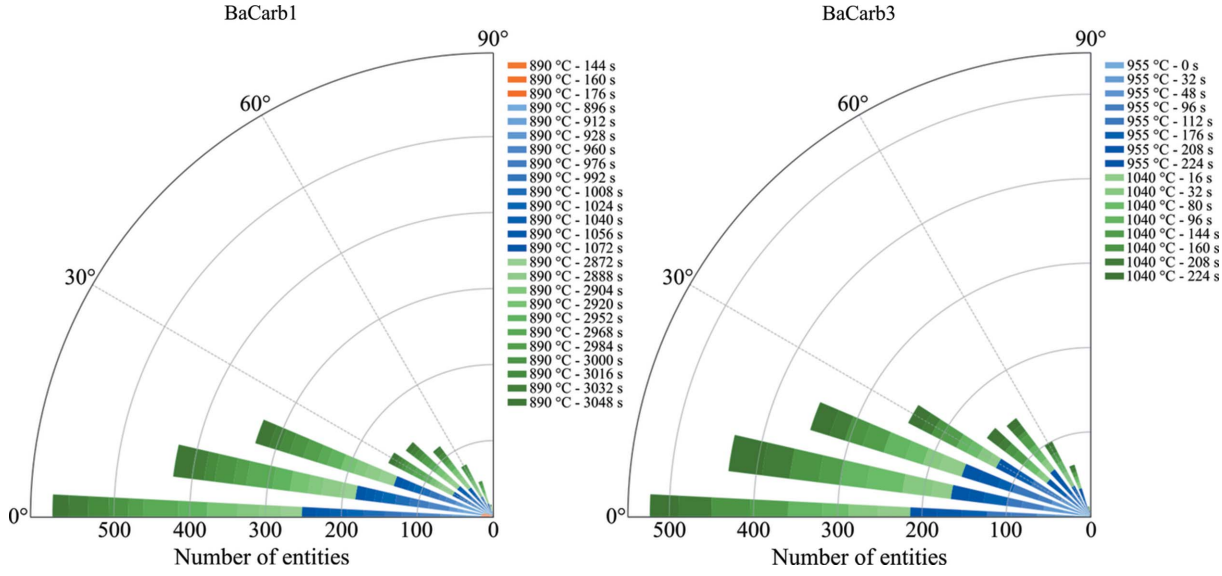

Figure 10
Orientation analysis through time. Each rose diagram represents the cumulative evolution of the dip angle relative to the *XY* plane for an experiment. 90% of BaCarb1 and BaCarb3 entities have orientation values under 48° and 51°, respectively.

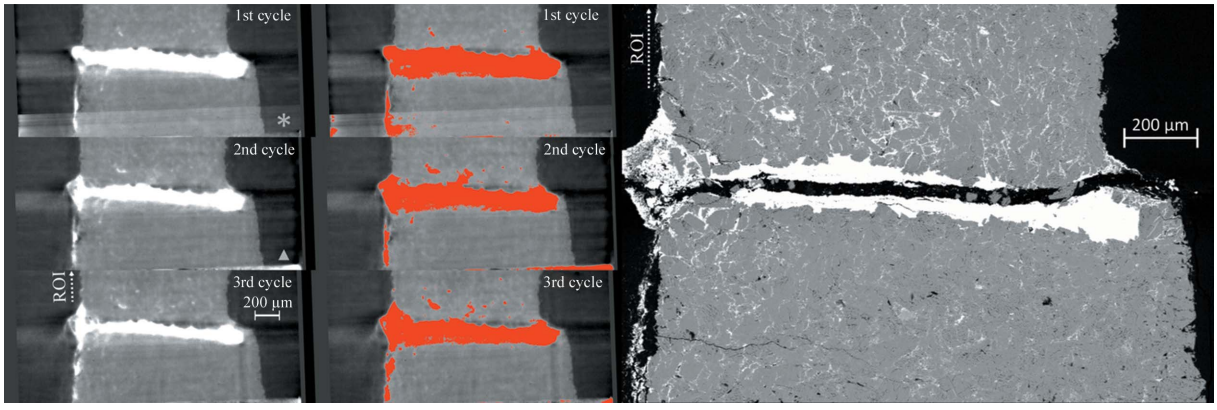

Figure 11
(Left and middle) Representative sections of XCT reconstructions over cycles 1, 2 and 3 for BaCarb1 and their corresponding segmentation, showing the progressive infill of the polycrystalline olivine (in grey) by the carbonate melt (in white). The asterisk (*) corresponds to an overilluminated part of the tomograph. The white solid triangle corresponds to the top of the anvil. The vertical position of the BaCarb1 cylindrical ROI is represented on both XCT and SEM images, its top extremity exceeding these images by dozens of micrometres. (Right) An SEM image of the same section on the quench, showing complete wetting of the porosity with submicrometre carbonate films surrounding olivine grains. Given the spatial resolution of XCT (4–5 µm) only the large melt blobs are identified, but nevertheless they can be tracked *in situ* with a time resolution of a few seconds for dynamic studies.

2016) to extreme conditions opened up by the UToPEc device offers an ideal approach for imaging these mass exchange processes. Although the spatial resolution is currently limited to 4–5 µm, which is significantly larger than what can be achieved with electron imaging, and depends on the absorption contrasts within the studied materials (Fig. 11), it allows *in situ* observations with an unprecedented time resolution for a quantitative understanding of reactive transport.

5. Conclusions

Here, we have reported the experimental setup developed on the PSICHE beamline at SOLEIL to perform high-speed XCT in the Ultra-fast Tomography Paris–Edinburgh cell (UToPEc) under extreme conditions of up to 10 GPa and 1700°C. We have provided a workflow for the acquisition, visualization and quantification of CT scans, accounting for the specific requirements of working in a high-pressure and high-temperature environment, and showed that alignment of time-lapse XCT reconstructions allows investigation of 3D volumes, morphological statistics and entity tracking through time. We have illustrated the potential of this 4D tomography technique through the example of magma impregnation, in which we were able to capture the capillary infiltration dynamics, under conditions of ∼2 GPa and $T > 800$°C, with micrometric resolution and characteristic times of a few seconds, as we tracked the melt propagation front and the gradual porosity filling, as well as fast chemical reactions. This breakthrough in 4D tomography opens new perspectives to explore the dynamics of phase transformations, reaction

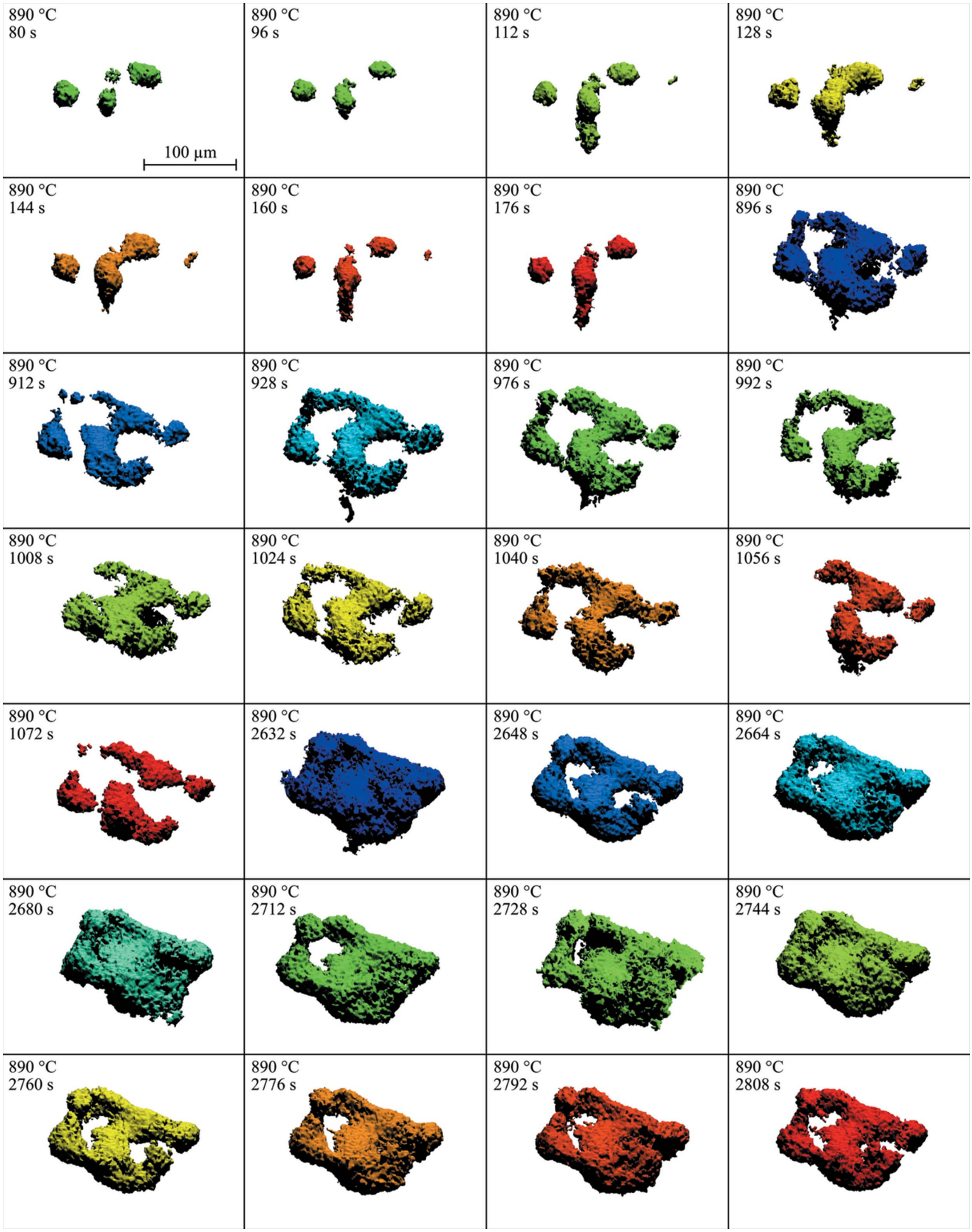

Figure 12
Tracking of the reaction rim surrounding a pyroxene grain in sample BaCarb1. Each caption represents the state of the system at a given time. Conditions are given in the upper left-hand corner of each panel.

kinetics and microstructures, as well as porosity flows under extreme conditions.

Acknowledgements

We thank G. Hamel, A. Prat and G. Morard for their collaboration on this project. This paper was improved by wise comments and suggestions from two anonymous reviewers.

Funding information

The UToPEc ongoing development programme is supported by DIM OxyMORE Île de France, Synchrotron SOLEIL and a CNRS-MITI grant.

References

Álvarez-Murga, M., Perrillat, J. P., Le Godec, Y., Bergame, F., Philippe, J., King, A., Guignot, N., Mezouar, M. & Hodeau, J. L. (2017). *J. Synchrotron Rad.* **24**, 240–247.

Boulard, E., Denoual, C., Dewaele, A., King, A., Le Godec, Y. & Guignot, N. (2020). *Acta Mater.* **192**, 30–39.

Boulard, E., King, A., Guignot, N., Deslandes, J.-P., Le Godec, Y., Perrillat, J.-P., Clark, A., Morard, G. & Itié, J.-P. (2018). *J. Synchrotron Rad.* **25**, 818–825.

Dobson, D. P., Jones, A. P., Rabe, R., Sekine, T., Kurita, K., Taniguchi, T., Kondo, T., Kato, T., Shimomura, O. & Urakawa, S. (1996). *Earth Planet. Sci. Lett.* **143**, 207–215.

Dobson, K. J., Coban, S. B., McDonald, S. A., Walsh, J. N., Atwood, R. C. & Withers, P. J. (2016.). *Solid Earth*, **7**, 1059–1073.

Godec, Y. L., Martinez-Garcia, D., Mezouar, M., Syfosse, G., Itié, J.-P. & Besson, J.-M. (2000). *High. Press. Res.* **17**, 35–46.

Green, D. & Wallace, M. (1988). *Nature*, **336**, 459–462.

Guignot, N., King, A. & Boulard, E. (2020). *J. Appl. Phys.* **127**, 240901.

Hammouda, T. & Laporte, D. (2000). *Geology*, **28**, 283–285.

Hunter, R. H. & McKenzie, D. (1989). *Earth Planet. Sci. Lett.* **92**, 347–356.

King, A., Guignot, N., Deslandes, J.-P., Pelerin, M., Joosten, I., De Looff, D., Li, J., Bertrand, L., Rosenberg, E., Dewaele, A., Boulard, E., Le Godec, Y., Perrillat, J.-P., Giovenco, E., Morard, G., Weitkamp, T., Scheel, M., Perrin, J., Chevreau, H. & Itié, J.-P. (2019). *Integr. Mater. Manuf. Innov.* **8**, 551–558.

Klotz, S., Hamel, G. & Frelat, J. (2004). *High. Press. Res.* **24**, 219–223.

Kono, Y., Kenney-Benson, C., Hummer, D., Ohfuji, H., Park, C., Shen, G., Wang, Y., Kavner, A. & Manning, C. E. (2014). *Nat. Commun.* **5**, 5091.

Liu, H., Wang, L., Xiao, X., De Carlo, F., Feng, J., Mao, H. & Hemley, R. J. (2008). *Proc. Natl Acad. Sci. USA*, **105**, 13229–13234.

Maire, E. & Withers, P. J. (2014). *Int. Mater. Rev.* **59**, 1–43.

Mao, W. L., Lin, Y., Liu, Y. & Liu, J. (2019). *Engineering*, **5**, 479–489.

Mirone, A., Brun, E., Gouillart, E., Tafforeau, P. & Kieffer, J. (2014). *Nucl. Instrum. Methods Phys. Res. B*, **324**, 41–48.

Paganin, D., Mayo, S. C., Gureyev, T. E., Miller, P. R. & Wilkins, S. W. (2002). *J. Microsc.* **206**, 33–40.

Perrillat, J. P. (2008). *Miner. Mag.* **72**, 683–695.

Philippe, J., Le Godec, Y., Mezouar, M., Berg, M., Bromiley, G., Bergame, F., Perrillat, J. P., Alvarez-Murga, M., Morand, M., Atwood, R., King, A. & Régnier, S. (2016). *High. Press. Res.* **36**, 512–532.

Rasband, W. S. (1997–2018). *ImageJ*. US National Institutes of Health, Bethesda, Maryland, USA (https://imagej.nih.gov/ij/).

Renard, F., Cordonnier, B., Dysthe, D. K., Boller, E., Tafforeau, P. & Rack, A. (2016). *J. Synchrotron Rad.* **23**, 1030–1034.

Stevenson, D. J. (1986). *Geophys. Res. Lett.* **13**, 1149–1152.

Turpin, L., Roux, S., Caty, O. & Denneulin, S. (2020). *Fundament. Inf.* **172**, 203–219.

Urakawa, S., Terasaki, H. P., Funakoshi, K., Uesugi, K. & Yamamoto, S. (2010). *J. Phys. Conf. Ser.* **215**, 012026.

Wang, Y., Uchida, T., Westferro, F., Rivers, M. L., Nishiyama, N., Gebhardt, J., Lesher, C. E. & Sutton, S. R. (2005). *Rev. Sci. Instrum.* **76**, 073709.

Washburn, E. W. (1921). *Phys. Rev.* **17**, 273–283.

Watson, E. B., Sneeringer, M. A. & Ross, A. (1982). *Earth Planet. Sci. Lett.* **61**, 346–358.

Yu, T., Wang, Y. & Rivers, M. L. (2016). *Prog. Earth Planet. Sci.* **3**, 17.